Ghost of Melts Past Beneath an Active Plate Boundary

R. E. Bernard[1,2], E. J. Chin[1], and C. Murphy[2]

[1] Scripps Institution of Oceanography, University of California, San Diego, La Jolla, CA, USA

[2] Amherst College, Amherst, MA, USA

Corresponding author: Rachel Bernard (rbernard@amherst.edu)

Key Points:

- Mid- lower crustal xenoliths from San Quintin in Baja California, Mexico characterized in terms of geochemistry and microstructure.
- Gabbroic xenoliths formed by underplated magma and record deformation in the presence of melt.
- Melt infiltration of pre-existing gabbros accommodated deformation in a deep crustal shear zone.

Abstract

We examine mid-lower crustal xenoliths erupted in Late Pleistocene to Holocene alkali basalt at San Quintin, Baja California, Mexico to investigate the role of partial melt in deep lithospheric deformation. Using major and trace element mineral chemistry data obtained from LA-ICP-MS and microstructural data obtained from EBSD, we cluster the crustal xenoliths into two groups based on textural and geochemical characteristics: Group (1) largely unfoliated two-pyroxene gabbros with minor amounts of olivine, and Group (2) gabbros with strong compositional foliation and up to 30% modal olivine. We interpret Group 1 xenoliths as representing underplated cumulates from basaltic magmas, whereas petrographic and quantitative microstructural data suggest Group 2 xenoliths record melt infiltration of pre-existing gabbros coeval with deformation, perhaps in a deep crustal shear zone. We propose this shear zone represents a deep lithospheric expression of the active transform plate boundary along the Baja California margin.

Plain Language Summary

Xenoliths, rock fragments brought up rapidly to the surface by volcanism, provide a unique, direct window into the nature of the deep lithosphere. Here we use xenoliths from the San Quintin Volcanic Field to explore the role melt (magma) plays in deformation. Geochemistry and analysis of the mineral textures within these rocks reveal two groups of xenoliths sourced from the lower crust: one formed from accumulation of magma in the lower crust, and another formed from the infiltration of melt into preexisting crustal rocks that were deformed during or prior to this melt infiltration.

1 Introduction

Plate tectonics is governed by the underlying idea that lithospheric plates are rigid and localize strain in narrow, well-defined zones. While this approximation is borne out amongst most lithospheric plates on Earth, some plate boundaries defy this behavior, defined instead by wide zones of seismicity and deformation (Gordon, 1998). A classic example of one such “soft”

margin is the Western US and Baja California, which is characterized by widespread low-velocity mantle, magmatism, and anomalous seismicity (Suppe et al., 1973).

Strike slip faulting plays a significant role in accommodating motion between plates (Woodcock, 1986), and characterizes much of the present-day North America-Pacific Plate margin. Seismic data indicates that large continental strike slip faults, such as the San Andreas Fault system extending along the entire California margin, may continue well into the lower crust (Henstock et al., 1997) and even the upper mantle (Ford et al., 2014). A major unresolved question is how deformation is distributed with depth and localized in the lithosphere. As temperature and pressure increase with depth in the crust and upper mantle, deformation shifts from brittle, narrow faults to ductile, wide shear zones (Fossen and Cavalcante, 2017; Wilson et al., 2004). Moreover, increasing temperature with depth brings rocks closer to their melting point, and so the role of partial melt becomes increasingly important in deep shear zones (Davidson et al., 1994; Holtzman and Kendall, 2010). Even a small fraction of melt may be important for lubricating the base of plate boundaries on a global scale (Schmerr, 2012; Tharimena et al., 2017). Despite recognition of the role of melt in deep lithospheric deformation, few direct observations exist because of the transitory nature of partial melt in the rock record.

2 Geologic Background

Xenoliths – fragments of deep lithospheric rocks brought up rapidly to the surface by volcanism – provide a unique window into deep lithospheric deformation. Here we examine mid-lower crustal xenoliths erupted in Late Pleistocene to Holocene basaltic cinder cones of OIB affinity at San Quintin, Baja California, Mexico (Luhr et al., 1995) **(Fig. 1)**. The xenoliths were sourced from the three localities within the San Quintin volcanic field with previously documented xenoliths: Basu, Woodford, and Media Luna (Luhr et al., 1995) **(Fig. 1)**. These volcanoes erupted close to the Santillan Y Barrera Line, which has been proposed as a potential fault-line structure (Gastil et al., 1975), and which may still be active: In 1975, a swarm of earthquakes occurred ~35 km northwest of the San Quintin volcanic field, which led to speculation of a possible NW trending transcurrent fault in the area (Rebollar et al., 1982). The volcanoes at San Quintin are unique amongst the extensive post-subduction magmatism of Baja California in being the only known source of lower crustal and upper mantle xenoliths along the peninsula.

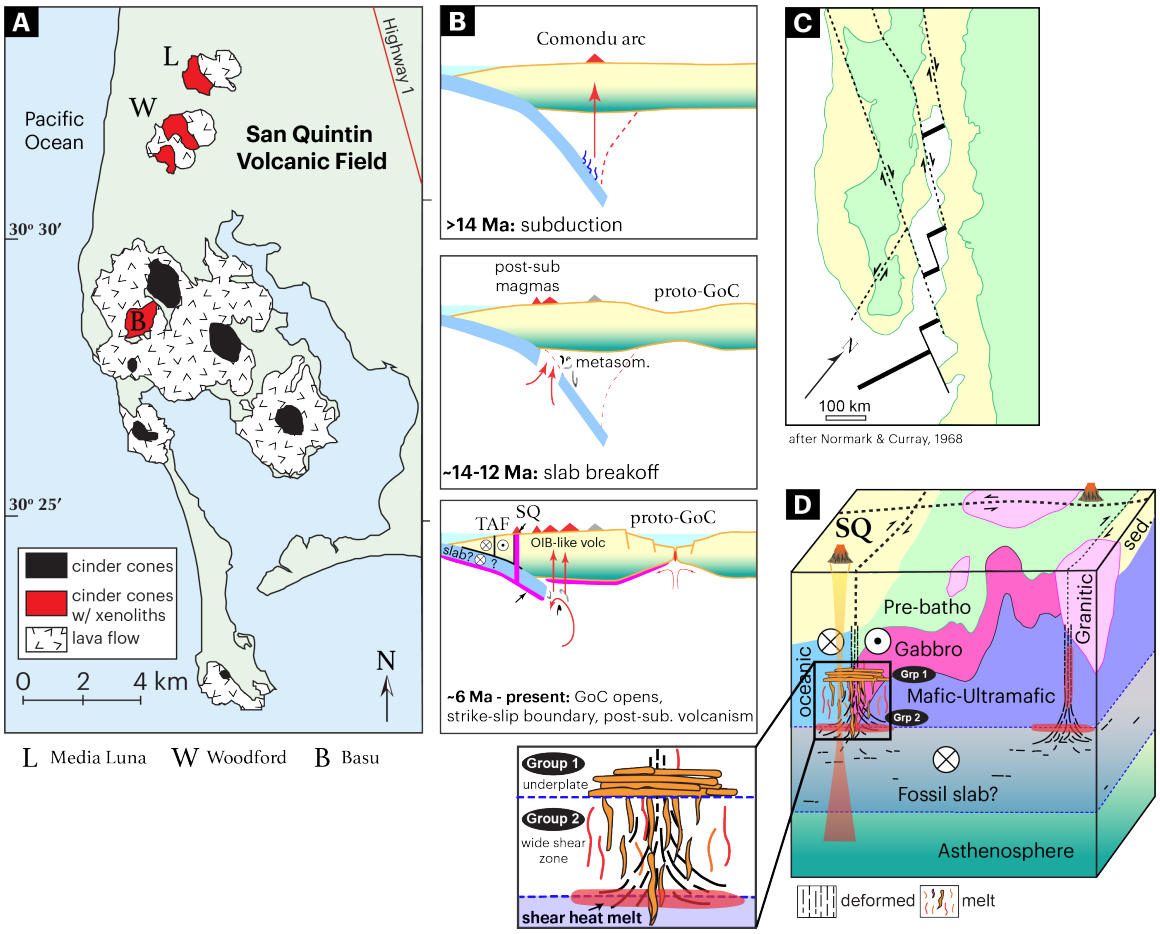

Figure 1: Geologic setting and geodynamic overview of Baja California. A) Simplified map showing locations of volcanic features in the San Quintin Volcanic Field. The three Holocene cinder cones (M = Media Luna, W = Woodford, B = Basu) containing mantle and lower crustal xenoliths are shown in red. B) Schematic cross-sections showing development of the Baja California plate margin. >14 Ma, Baja was part of the Comondu arc along mainland Mexico. Between ~14 and 12 Ma, the margin transitioned out of subduction to rifting and initial opening of the Gulf of California. Slab window opens, post-subduction alkaline magmatism follows. From ~6 Ma to present, Gulf of California continues to open, strike-slip plate boundary develops, and post-subduction alkaline magmatism continues. Magenta layer represents hypothetical low-degree melt layer**.** C) Map view of one possible tectonic reconstruction of Baja California rifting from the mainland accommodated by a series of transcurrent faults coeval with the opening of the Gulf of California. D) Schematic block diagram showing tectonic and petrologic relationships as well as two possible melt sources. Group 1 xenoliths precipitate from crustally-derived melt, whereas Group 2 xenoliths are sourced slightly deeper and both Group 1 and 2 xenoliths are carried to the surface by a deeper-sourced melt that could be shear heating related.

San Quintin mantle xenoliths are well-studied examples of peridotite that experienced significant plastic deformation and are renowned for their strongly porphyroclastic, highly strained textures (Basu, 1977b). These deformed peridotites show strong olivine crystallographic preferred orientation (CPO) and evidence of melt-rock reaction, which Cabanes and Mercier (1988) and Palasse et al. (2012) interpreted as evidence for intense deformation in a shallow shear zone in the upper mantle. Similarly strong olivine CPOs consistent with formation

at high temperatures and high average shear wave anisotropy have been reported in xenoliths from beneath the San Andreas Fault system, suggesting that the fault shear zone extends to at least 40 km depth (Titus et al., 2007). While San Quintin mantle xenoliths have been the subject of several studies (Bacon and Carmichael, 1973; Basu, 1977a, b, 1979; Cabanes and Mercier, 1988; Palasse et al., 2012), only one published work on the fabrics of deep crustal xenoliths exists to date (van der Werf et al., 2017). This study by van der Werf et al. (2017) examined the rheological properties of San Quintin granulites and lherzolites, finding microstructures consistent with deformation occurring at very low differential stresses in both the uppermost lower crust and upper mantle via a combination of dislocation and grain-size-sensitive creep.

We present new mineral chemistry data on 11 lower crustal xenoliths, 10 of those for which we also present microstructural analysis (detailed microstructural analyses of three samples are the primary focus). Despite displaying a wide range of igneous and deformational textures, lower crustal xenoliths consistently contain plagioclase, clinopyroxene, orthopyroxene, spinel (oxides), and olivine. Our studied samples fall into two groups (Group 1 and 2) based on textural and geochemical characteristics, which we discuss in the next sections.

3 Methods

Automated electron backscatter diffraction (EBSD) maps were acquired on an Oxford Instruments Symmetry EBSD detector on a FEI Apreo LoVac field emission gun scanning electron microscope (SEM) at the University of California San Diego (UCSD) using a step size of 3 – 15 μm, at a working distance between 26 to 28 mm, and voltage of 20 kV. Post-processing, including noise reduction with a smoothing spline filter, was done using the open source MTEX software (version 5.1.1) (Bachmann et al., 2011). MTEX was also used to generate and analyze the data as EBSD maps and pole figures. Contoured pole figures were generated using the density of the orientation distribution function (ODF) with a half-width of 10° plotted on the lower hemisphere. Grain boundaries are defined with a minimum angle of 10°. Internal distortions within grains are quantified using the built-in MTEX functions grain orientation spread (GOS) and Mis2Mean, both measured in degrees. Mis2Mean is the misorientation between each pixel in a grain and the mean orientation of that grain. GOS is the average Mis2Mean value of each grain (as an example, a grain with a high degree of internal

misorientation would have a high GOS). The strength of the CPO was quantified using the dimensionless J-index, which varies from 1 (random orientation) to infinity (Bunge, 1982; Mainprice et al., 2015). MTEX was also used to investigate shape preferred orientation (SPO) by identifying the long axes of each grain within the mapped area and plotting the frequency of their orientation relative to the horizontal as rose diagrams.

Major and trace elements were collected from polished thin sections using a Thermo Fisher Scientific iCAP Qc Inductively Coupled Plasma Mass Spectrometry (ICP-MS) with New Wave Research UP213 Laser Ablation system at UCSD. A laser spot size of 100 μm and a 5 Hz repetition rate with a fluence of 3-3.5 J/cm^2 was used. For each spot, measurements were taken for 60 seconds. Data was calibrated for each session (before, during, and after analyses of unknowns) using the standard reference glasses NIST612, NIST610, BHVO-2g, BCR-2g, and BIR-1g, and then corrected using Ca as the normalizing element.

Following LA-ICP-MS work, minerals were analyzed for major elements and WDS maps were collected using the Cameca SX-100 electron microprobe with a CeB6 filament and 5 WDS detectors at University of California Santa Barbara (20kV voltage, 10 nA beam current, 2 μm spot size) using in-house standards. Additional data from one sample (THSQ4) was collected using the Cameca SXFive-TACTIS microprobe with 5 WDS detectors and in-house standards at the University of Massachusetts at Amherst (15kV, 20 nA, 2 μm). WDS mapping data were input into XMapTools software (version 3.4.1) to calculate volume modal percentages using representative points for each phase (Lanari et al., 2019).

4 Results

4.1 Microstructures

Group 1 consists of generally unfoliated, occasionally poikilitic two-pyroxene gabbros (with minor olivine) exhibiting weak or no foliation (see Fig. S1 and Table S1 in the Supplement for photomicrographs and details on petrographic characteristics, mineral modes, and average mineral grain sizes). Some Group 1 gabbros are equigranular but with a shape-preferred orientation (SPO) characterized by elongated plagioclase and/or pyroxenes defining a weak foliation. The plagioclase and clinopyroxene grains often appear cotectic in these samples. Group 2 consists of two-pyroxene gabbros with up to ~30% modal olivine (Fig. 2, Fig. S1, Table S1).

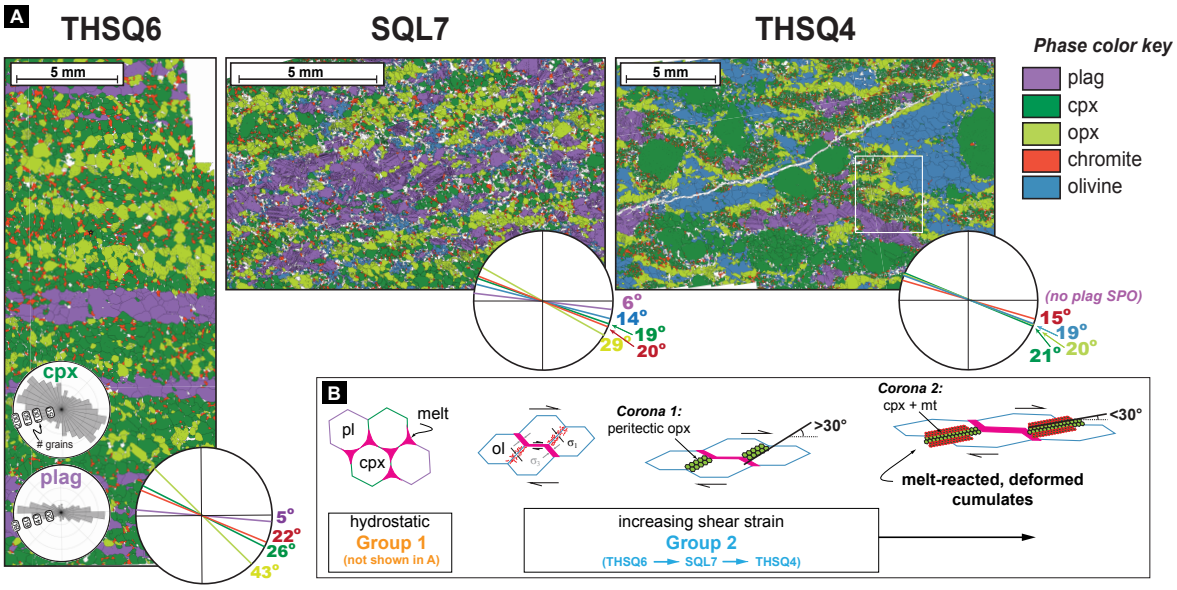

Figure 2: EBSD phase maps and diagrams of three Group 2 xenoliths. Rose diagrams, shown in two examples for sample THSQ6 (bottom left), were generated from EBSD data; the numbers on concentric circles represents a count of grains and the placement of the bars along those circles reflects the degrees between the orientation of a grain's long axis and the map's horizontal direction. Simplified versions (without concentric circles or bars) are shown in larger circles for each sample to illustrate the average offset (in degrees) between the grain long axes and foliation trace (horizontal). Rose diagrams for all phases in these samples are in the Supplement. The white rectangle in the THSQ4 phase map is the mapped area for **Fig. 3**. B) Conceptual model based on the experimental findings of Soustelle et al. (2014).

Texturally Group 2 differs from Group 1 samples in that the former are characterized by strong compositional layering grading into disrupted layering with complex coronas mantling clinopyroxene and olivine (Fig. 2). A multi-layered corona is shown in detail in Fig. 3, where the first orthopyroxene corona mantles olivine, followed by a second corona around orthopyroxene comprised of symplectite of fine-grained clinopyroxene and spinel.

Microstructures preserved in both Group 1 and 2 xenoliths record varying degrees of deformation, due to both magmatic and solid state processes. Despite a weak SPO-defined foliation, some Group 1 xenoliths have significant CPOs (Fig. S2). However, the generally low internal grain misorientations and straight or curvilinear grain boundaries (Fig. S3, S4), supports a magmatic – rather than crystal-plastic – origin to the weak foliation and/or CPO preserved in Group 1 samples. This is also reinforced by the CPO types preserved in some Group 1 samples. In THSQ2a, for example, plagioclase displays a CPO pattern consistent with axial-B or (010)-fiber CPO, characterized by girdles within the foliation plane of [100] and (001), and (010) point maxima oriented normal to foliation (Fig. S2). This CPO is common for plagioclase, thought to be associated with magmatic, rather than solid state, deformation (Satsukawa et al., 2013). The

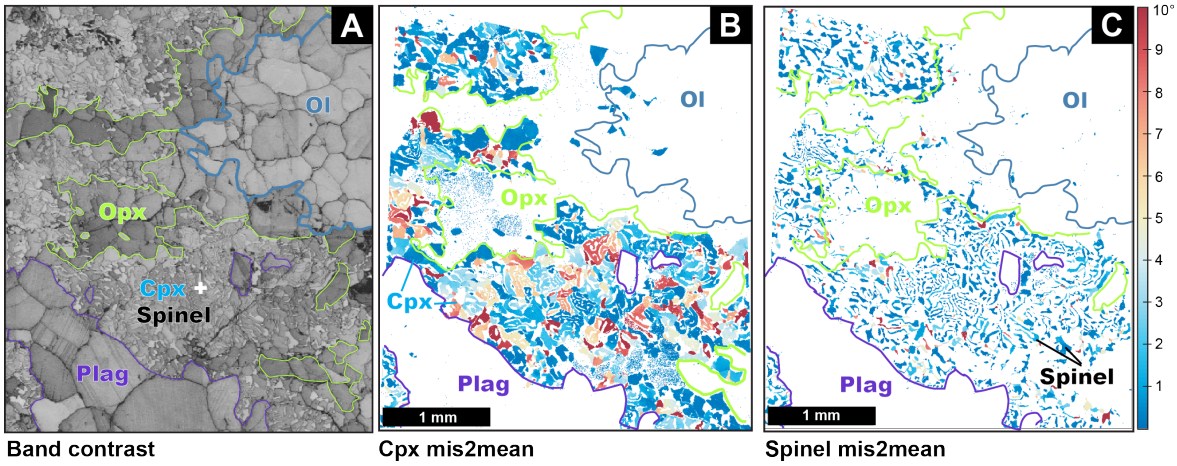

Figure 3: Higher resolution EBSD map (5 µm step size) of THSQ4 (rectangular area in Fig. 2a). A) Band contrast map; B-C) Mis2mean map of symplectite corona for clinopyroxene only (B) and spinel only (C).

straight or curvilinear grain boundaries and generally low internal misorientation also supports a magmatic origin to any weak foliation or CPO preserved in Group 1 samples. SQW9, on the other hand – a sample with lath-shaped olivine grains intergrown with plagioclase and clinopyroxene surrounding clinopyroxene cores (Fig. S3) – is an outlier among Group 1 samples with its strong intragranular misorientations in orthopyroxene and clinopyroxene grains and its preservation of plagioclase type-P CPO, associated with plastic deformation (Satsukawa et al., 2013). The orthopyroxene appears to have replaced clinopyroxene – an observation based on textural relationships (orthopyroxene forming on the edges of clinopyroxene grains) and identical orthopyroxene-clinopyroxene CPOs characterized by point maxima of [100] normal to foliation, weak alignment of [010], and a girdled [001] within the foliation plane.

Group 2 samples show stronger compositional layering and significant SPO in clinopyroxene, orthopyroxene, spinel, and olivine. Plagioclase rarely displays an SPO, and instead appears as polygonal with straight grain boundaries and triple junctions**.** Some Group 2 samples, such as the strongly layered THSQ6, have no significant internal misorientation as evident from the low GOS distribution across all grain sizes (Fig. 4, Fig. S4), and little to no CPO in any phases (J indices < 2) (Fig. S2), but marked SPO in all minerals except plagioclase (Fig. 2). Another feature of plagioclase in THSQ6 is abundant quadruple grain junctions, which can be diagnostic of grain boundary sliding (Ashby and Verrall, 1973). Other Group 2 samples, particularly those with greater olivine modes – such as SQL7 and THSQ4 – appear more deformed, as they display strong SPO, moderate to strong internal misorientations in olivine and

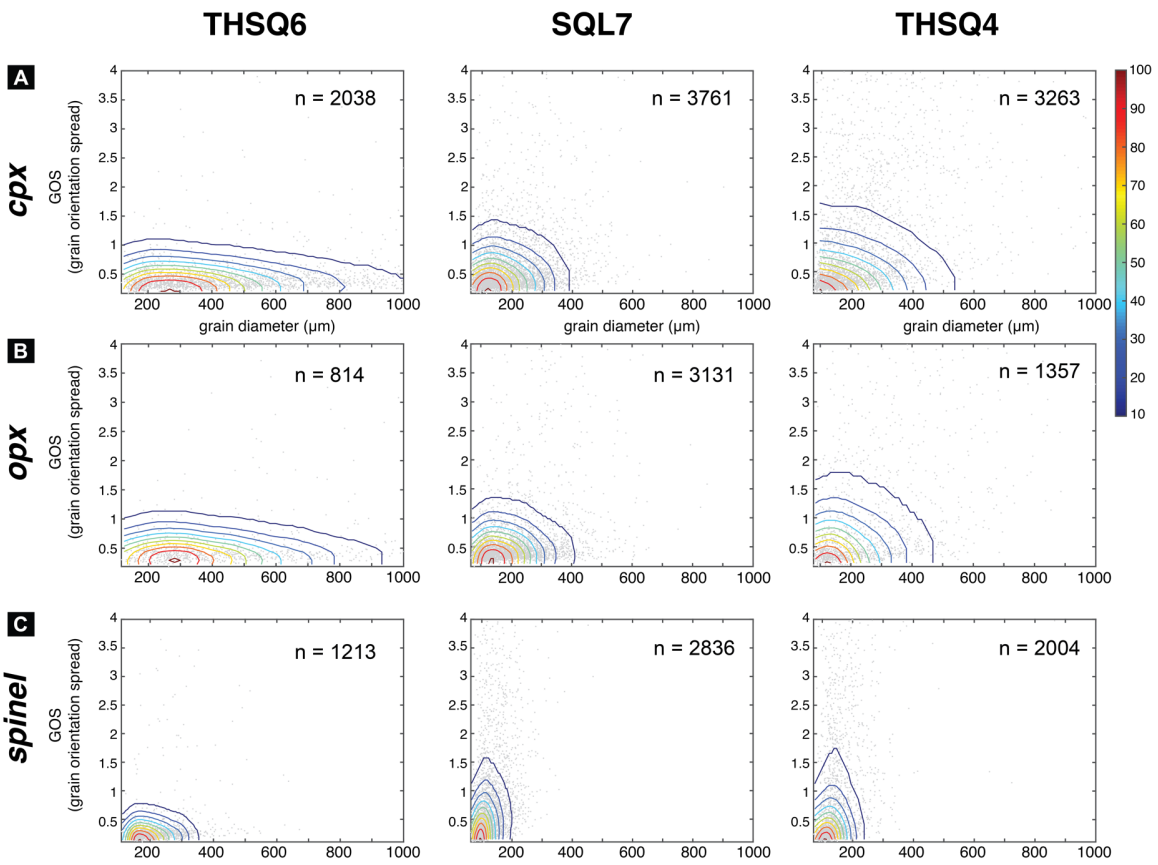

Figure 4: Grain orientation spread (GOS) vs. grain size for (A) clinopyroxene, (B) orthopyroxene, and (C) spinel in the three representative samples from Fig. 2. Individual data points shown in gray overlain by colored density contours. THSQ6 has a wider range of grain sizes and lower GOS in all phases, consistent with the interpretation that it is the least deformed of the three. THSQ4 has higher GOS values, consistent with the interpretation that it is the most deformed.

pyroxenes, moderate CPOs (J indices range from 1 to 4), and higher mineral GOS distribution across all grain sizes (Fig. 4, Fig. S2, S4).

Interestingly, samples with coronas of clinopyroxene-spinel symplectites show significant internal misorientations within the clinopyroxene (Fig. 3), suggesting deformation occurred either after or during corona formation. THSQ4 is a particularly good example of this; the symplectite clinopyroxene shows significantly greater internal deformation than the large, relict clinopyroxenes outside of these symplectite layers (Fig. S5). This symplectite is the outer layer of corona lenses, which themselves appear elongated in the lineation direction. Deformation within the corona olivine has a strong CPO, SPO, and irregular grain boundaries (Fig. S6).

4.2 Mineral Chemistry

We report incompatible trace element concentrations of orthopyroxenes (Table S2) and clinopyroxenes (Fig. 5, Table S3), normalized to primitive mantle (McDonough and Sun, 1995), for Group 1 and 2 crustal xenoliths and two San Quintin mantle xenoliths. Lower crustal xenolith Group 1 is characterized by overall more enriched compositions (up to 10x primitive mantle) compared to Group 2. Both groups have generally flat rare earth element (REE) patterns and negative anomalies in Nb and Zr. Group 1 has a negative Sr anomaly (with respect to Ce and Nd), whereas Group 2 xenoliths have positive Sr anomaly. This is more clearly shown in Fig. 5 where Group 1 clinopyroxenes have low Ti/Sm and low Sr/Nd, but Group 2 have elevated Ti/Sm and Sr/Nd.

We analyzed major element compositions of clinopyroxene in the Group 2 xenoliths THSQ6, SQ4 (texturally similar to SQL7), and THSQ4 and olivine in THSQ4 (Table S4). Clinopyroxene in THSQ6 and SQ4 are homogeneous with respect to core-rim variation, with average Mg# of 82 and 81, respectively. In contrast, THSQ4 clinopyroxene porphyroclast cores have slightly lower Mg# (83) and CaO (19 wt.%) compared to rims (Mg# 85; CaO 23 wt.%). Olivine has an average Mg# of 76.

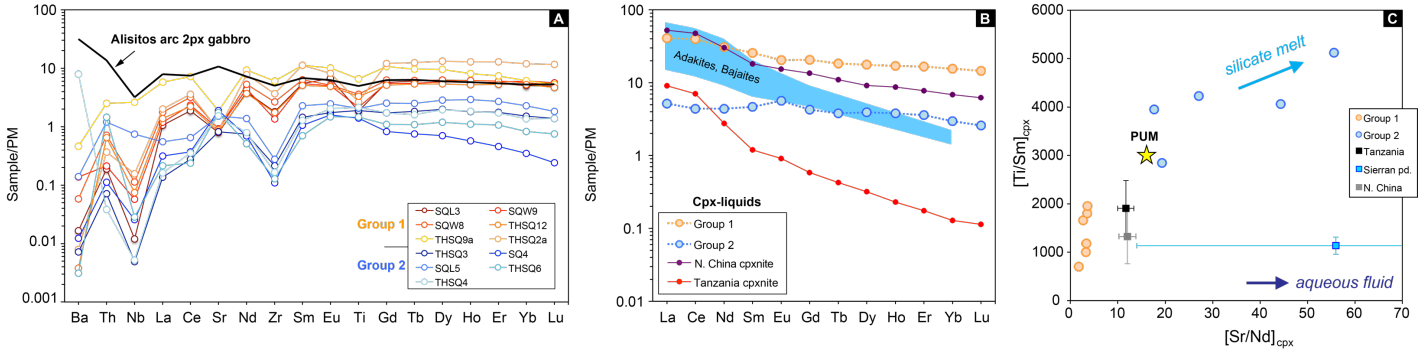

Figure 5: Clinopyroxene trace element geochemistry. A) Primitive mantle-normalized incompatible element diagram plotting Group 1 and Group 2 xenoliths. Two-pyroxene gabbro of the Alisitos arc is also shown (data from Morris et al. (2019)). B) Primitive mantle-normalized rare earth element (REE) diagram showing calculated liquids in equilibrium with clinopyroxenes using partition coefficients from Kelemen et al. (2003). Also shown for comparison are melts in equilibrium with clinopyroxene from lower crustal pyroxenites from North China Craton Chin et al. (2020) and cumulate clinopyroxenites from Tanzania Chin (2018). Field of adakite and bajaite from Castillo (2008). C) Ti/Sm versus Sr/Nd in clinopyroxenes from Group 1 and Group 2 xenoliths.

200

201 **5 Discussion**

202 ***5.1 Textural analysis: Evolution of SPO and corona textures***

203 The compositional layering preserved in Group 2 rocks is often oblique to the elongation of
204 minerals within these layers. We show this quantitatively using rose diagrams that plot long axis
205 orientations of grains for each mineral. There is a clear, but variable, mineral SPO within Group
206 2 samples (Fig. 2, Fig. S7). Starting with the strongly layered sample THSQ6, orthopyroxene
207 SPO is highly oblique (43°) to the foliation (horizontal aspect of the map). Note the apparent
208 lack of olivine in THSQ6. With increasing modal olivine, the angle of orthopyroxene layering
209 decreases, as observed in SQL7 (29°) to THSQ4 (20°) (Fig. 2). The SPO of clinopyroxene and
210 spinel is also consistently oblique to foliation (~15-25°), though to a lesser extent than
211 orthopyroxene on average. In contrast, plagioclase layers remain more or less parallel with
212 foliation (within ~5°).

213 Interestingly, the amount of offset between orthopyroxene SPO and foliation appears to
214 be a function of degree of strain, as shown quantitatively by GOS versus grain size plots (Fig. 4).
215 In fact, with increasing disruption of the macro-scale layering across the three xenoliths in Fig. 2,
216 all corona minerals (orthopyroxene, clinopyroxene, spinel) transition from a wide grain size
217 distribution at consistently low GOS (i.e., all grains, regardless of size have little internal
218 misorientation) to a narrow grain size distribution extending to higher GOS (i.e., smaller and
219 more internally distorted grains) (Fig. 4).

220 The systematic variation in SPO angle with respect to foliation and concomitant increase
221 of intragrain strain is strikingly similar to fabric evolution observed in experimentally deformed
222 olivine + melt aggregates (Soustelle et al., 2014). Under hydrostatic conditions, the experiments
223 show melt homogeneously distributed along olivine grain boundaries – e.g., similar to the texture
224 of cumulate gabbros with interstitial crystallized melt, as represented by the Group 1 xenoliths.
225 Soustelle et al. (2014) found that, with increasing shear strain, the melt + olivine aggregate
226 experiences progressive melt-rock reaction and melt segregation into opening grain boundaries.
227 Counteracting this is development of high dislocation density along grain boundaries compressed
228 by the deformation; peritectic formation of orthopyroxene is favored along such boundaries.

With increasing shear strain, the orientation of peritectic orthopyroxene aligns with the shear direction.

5.2 Nature of the melt

Silica-saturated (tholeiitic) basalts show the peritectic relationship Mg_2SiO_4 (olivine) + SiO_2 (melt) → $Mg_2Si_2O_6$ (orthopyroxene) at low pressure and dry conditions. The gabbroic mineralogy of the San Quintin xenoliths indicates crystallization from basaltic melts. Yet, constraints on the last equilibration P-T of the xenoliths indicates relatively deep conditions – two-pyroxene geothermometry and phase equilibria modeling record last equilibration in the mid to lower crust at 750 – 890 °C and 400 – 560 MPa (15-22 km) (van der Werf et al., 2017). Further supporting a hot, high pressure origin, apparent partition coefficients (D_{REE}) between orthopyroxene and clinopyroxene fall along the high-temperature equilibrium line (Lee et al., 2007) (Fig. S8). These REE-based temperatures overlap those calculated for San Quintin mantle xenoliths (Fig. S8), which have also been interpreted to be melt-refertilized (Palasse et al., 2012). Given these near-solidus conditions for both the upper mantle and lower crust, and the similarity to melt-present deformation experiments of Soustelle et al. (2014) discussed above, we interpret the peritectic coronas in the San Quintin xenoliths as the product of mantle-derived, basaltic melt crystallization coeval with deformation in the mid to lower crust.

However, at high pressure (1.5 GPa) and dry conditions, the peritectic reaction in tholeiitic basaltic compositions disappears (Chen and Presnall, 1975). The addition of water to the system at high pressure resurrects the peritectic reaction, and also expands the liquidus field of clinopyroxene (Kushiro and Yoder, 1969). These phase equilibria could explain the corona sequence of first orthopyroxene rimming olivine followed by clinopyroxene (+ spinel) (Fig. 3). We propose that this corona sequence could develop during progressive crystallization of interstitial, moderately hydrous melt as the cumulate cooled (de Haas et al., 2002; Joesten, 1986; Otamendi et al., 2010). Unlike some of the coronas observed by Otamendi et al. in Famatina arc cumulates, the San Quintin xenoliths lack an outer amphibole-rich corona, suggesting that the melt was not as hydrous as those found in subduction zones.

Together with their typical cumulate fabrics, Group 1 xenoliths may represent underplated cumulates from basaltic magmas, whereas the variably layered to distrupted, coronitic textures of Group 2 record melt infiltration into pre-existing gabbros coeval with

deformation, perhaps in a deep crustal shear zone (Fig. 1d). Layered gabbros from Group 2, such as THSQ6, could represent former Group 1 gabbros which were subsequently melt-reacted and deformed; this transition is represented in SQL7 to THSQ4. Indeed, the Mg# of coexisting olivine and clinopyroxene "paleoclasts" (i.e., large, relict grains not in coronas) show disturbed equilibrium compared to olivine-clinopyroxene Mg# in layered gabbros (Lissenberg and Dick, 2008) (Table S4). This could be due to progressive reaction of paleoclasts with melt to form complex coronas.

6 Geologic Interpretations

Petrographic and quantitative microstructural data support melt infiltration and deformation occurring contemporaneously in San Quintin Group 2 lower crustal xenoliths. The timing of these events, however, is not well constrained owing to lack of published radiometric age data on the xenoliths. Based on geologic and tectonic context, two possibilities exist (cf.van der Werf et al., 2017): 1) The xenoliths represent lower crust originally sourced from the North American mainland (i.e. present-day Mexico) that rifted to the present day location of Baja California during the Neogene – present opening of the Gulf of California, or 2) the xenoliths represent more recent crust of either Pacific or North American heritage, deforming along the still active transform plate boundary.

In the first scenario, the crust now represented by the San Quintin xenoliths could have been originally associated with the long-lived Cretaceous subduction zone that characterized much of the Western North American margin (Dickinson, 2004). The primitive mantle normalized incompatible trace element pattern of two-pyroxene gabbro from the Alisitos arc, formed during the Cretaceous in response to subduction beneath Mexico (Morris et al., 2019) shows a mild arc signature, e.g., enrichment in large-ion lithophile elements (Ba, Th, Sr) relative to fluid-immobile elements like Nb and Zr (Fig. 5). The rare earth elements are flat and similar to MORB, supporting the hypothesis that the Alisitos terrane was a thin, juvenile oceanic arc (Morris et al., 2019). Clinopyroxene trace element patterns of the San Quintin xenoliths, particularly the Group 2 xenoliths, differ from Alisitos two-pyroxene gabbro in having an overall more depleted (i.e., low Ba, Th, La) pattern (Fig. 5). We note, however, that side-by-side comparisons between the Alisitos plutonic arc rocks and xenoliths may be questionable, as deep

crustal xenoliths often trend towards more primitive compositions compared to exhumed lower crust (Rudnick and Fountain, 1995). Moreover, clinopyroxene trace elements have not been reported for Alisitos gabbros.

In the second scenario, "de novo" melt infiltration and shearing occurred concomitant with evolution of the transform plate boundary, with deformation along this boundary continuing into the lower crust and uppermost mantle (Cabanes and Mercier, 1988; Palasse et al., 2012; van der Werf et al., 2017) (Fig. 1d). Models of how the Baja terrane severed from the mainland and sutured to the Pacific Plate (Lonsdale, 1995) point to movement along *en echelon* strike-slip faults trending diagonal to the opening Gulf of California (Normark and Curray, 1968) (Fig. 1c). Evidence of an early major transform fault is suggested by the northwest-trending, ~400 km long Tosco-Abreojos (TAF) fault zone inferred to be active between 4.5 to ~12 My ago (Spencer and Normark, 1979). Modeling of interplate coupling by Plattner et al. (2009) indicates that a (minimum) shear stress of ~10 MPa along the TAF is reasonable for geological time scales; this stress overlaps the range of 12-33 MPa found by van der Werf et al. (2017) using recrystallized grain size paleopiezometry on San Quintin lower crustal xenoliths. Furthermore, fault activity occurs near San Quintin along the Agua Blanca fault system (Allen et al., 1960), and seismic activity ~30 km from San Quintin has occurred in the last few decades (Rebollar et al., 1982).

If the strike slip fault system accommodating Pacific-Baja plate movement does indeed continue into the ductile regime, deformation would be more widely distributed at depth. Geothermobarometry on San Quintin xenoliths by van der Werf et al. (2017) is consistent with a hot geotherm beneath Baja, and so rocks would be nearer to their solidus, supporting a role for melt-induced deformation in deep crustal shear zones. The question arises as to the geometry of such a deep lithospheric shear zone. Although absent from northern Baja, shear velocity anomalies at ~100 km depth have been interpreted as microplate remnants attached to the Baja lithosphere (Wang et al., 2013); modeling based on this hypothesis (Negrete-Aranda et al., 2013) proposed that shear heating along a low viscosity layer between the microplate and Baja lithosphere induced partial melting consistent with patterns of post-subduction volcanism in the region (e.g., Castillo, 2008). Rapid northwest movement of the Baja terrane could have dragged the microplate and the intervening low-viscosity layer with it (Pikser et al., 2012). Ongoing mantle upwelling in the Gulf of California would allow partial melt formed in the deep crust to have multiple pathways along either horizontal decollements (i.e., associated with coupling of

relict microplate lithosphere to Baja lithosphere) or localized, mostly vertical shear zones, perhaps reactived from inherited patterns of ancestral faulting associated with the opening of the Gulf and breakaway of the Baja terrane (Fig. 1d).

The two hypotheses outlined above are not mutually exclusive. The San Quintin xenoliths may have originated as pre-14 Ma arc lower crust, and either acquired their deformed state during active subduction or more recently as the transform boundary evolved. Age data on the San Quintin xenoliths would resolve the issue of an arc origin. Alternatively, the San Quintin xenoliths represent post-14 Ma oceanic mid to lower crust along a lithospheric boundary between the Pacific and Baja/North American plates, recently melt-infiltrated and deformed due to continuation of strike-slip faults into the deep lithosphere. Calculated melts in equilibrium with San Quintin clinopyroxenes suggest a MORB rather than subduction heritage (Fig. 5b). Furthermore, clinopyroxene Ti/Sm and Sr/Nd ratios show a trend where Group 1 clinopyroxenes have low Sr/Nd and low Ti/Sm whereas Group 2 clinopyroxenes have elevated Ti/Sm and high Sr/Nd (Fig. 5c). Metasomatism dominated by aqueous fluids would elevate Sr/Nd but not Ti/Sm, since Sr is highly fluid mobile but Ti is fluid immobile. As an example, clinopyroxene from refertilized peridotites from the Sierra Nevada paleo-arc (Chin et al., 2012) extend to very high Sr/Nd at low Ti/Sm, indicating interaction with subduction-derived melts and fluids. By contrast, clinopyroxenes from the East African Rift (Chin, 2018) plot at low Sr/Nd, indicating crystallization from or interaction with anhydrous melts. Group 2 San Quintin clinopyroxenes have both high Sr/Nd and high Ti/Sm, distinct from Sierran arc xenoliths. We therefore propose that melt rock interaction may have increased going from Group 1 to Group 2 xenoliths, but the metasomatism was primarily silicate melt-dominated with a negligible fluid component.

7 Conclusion

We report new EBSD-based microstructural data and mineral chemistry on lower crustal xenoliths from San Quintin, Baja California, Mexico. The xenoliths are categorized as Group 1 gabbronorites (<10% olivine, weak foliation and generally poikilitic textures, up to ~10x primitive mantle trace element concentrations) and Group 2 gabbronorites (>10 % olivine, an SPO that rotates with foliation, distinctive corona textures, and 1x or lower primitive mantle

trace element concentrations). We interpret Group 1 xenoliths as underplated cumulates of mantle-derived, basaltic melts, whereas Group 2 xenoliths represent melt-infiltrated gabbros from a deep crustal shear zone. Gradual rotation of SPO to align with foliation has been previously found to occur during deformation experiments on sheared olivine + melt aggregates. We also find that the extent of intragranular strain, exemplified in crystallized melt coronas, increases as SPO and foliation orientation coincide, further supporting that deformation and melt went hand-in-hand. Collectively, the textures and geochemistry of Group 2 xenoliths suggest that active strike-slip tectonics extends into the deep lithosphere, and that melt may play a key role in facilitating deformation.

Acknowledgments, Samples, and Data

The authors have no known conflicts of interest that could have influenced the work reported in this paper. This research was supported by a Scripps Postdoctoral Scholar award made to R. E. Bernard and Amherst College Greg S. Call Summer Student funding made to C. Murphy. Data presented in this manuscript can be accessed through the open access Zenodo repository (doi: 10.5281/zenodo.5213859).

References

Allen, C.R., Silver, L.T., Stehli, F.G., 1960. Agua Blanca fault—A major transverse structure of northern Baja California, Mexico. *Geological Society of America Bulletin* 71, 467-482.

Ashby, M., Verrall, R., 1973. Diffusion-accommodated flow and superplasticity. *Acta metallurgica* 21, 149-163.

Bachmann, F., Hielscher, R., Schaeben, H., 2011. Grain detection from 2d and 3d EBSD data: Specification of the MTEX algorithm. *Ultramicroscopy* 111, 1720-1733.

Bacon, C., Carmichael, I., 1973. Stages in the PT path of ascending basalt magma: an example from San Quintin, Baja California. *Contributions to Mineralogy and Petrology* 41, 1-22.

Basu, A.R., 1977a. Olivine-spinel equilibria in lherzolite xenoliths from San Quintin, Baja California. *Earth and Planetary Science Letters* 33, 443-450.

Basu, A.R., 1977b. Textures, microstructures and deformation of ultramafic xenoliths from San Quintin, Baja California. *Tectonophysics* 43, 213-246.

Basu, A.R., 1979. Geochemistry of ultramafic xenoliths from San Quintin, Baja California. *The mantle sample: inclusion in kimberlites and other volcanics* 16, 391-399.

Bunge, H., 1982. Texture Analysis in Materials Science. Butterworth's, London.

Cabanes, N., Mercier, J.-C., 1988. Insight into the upper mantle beneath an active extensional zone: the spinel-peridotite xenoliths from San Quintin (Baja California, Mexico). *Contributions to Mineralogy and Petrology* 100, 374-382.

Castillo, P.R., 2008. Origin of the adakite–high-Nb basalt association and its implications for postsubduction magmatism in Baja California, Mexico. *GSA Bulletin* 120, 451-462.

Chen, C., Presnall, D., 1975. The system Mg2SiO4-SiO2 at pressures up to 25 kilobars. *American Mineralogist* 60, 398-406.

Chin, E.J., 2018. Deep crustal cumulates reflect patterns of continental rift volcanism beneath Tanzania. *Contributions to Mineralogy and Petrology* 173, 85.

Chin, E.J., Lee, C.-T.A., Luffi, P., Tice, M., 2012. Deep Lithospheric Thickening and Refertilization beneath Continental Arcs: Case Study of the P, T and Compositional Evolution of Peridotite Xenoliths from the Sierra Nevada, California. *Journal of Petrology* 53, 477-511.

Chin, E.J., Soustelle, V., Liu, Y., 2020. An SPO-induced CPO in composite mantle xenoliths correlated with increasing melt-rock interaction. *Geochimica et Cosmochimica Acta* 278, 199-218.

Davidson, C., Schmid, S.M., Hollister, L.S., 1994. Role of melt during deformation in the deep crust. *Terra Nova* 6, 133-142.

de Haas, G.-J.L., Nijland, T.G., Valbracht, P.J., Maijer, C., Verschure, R., Andersen, T., 2002. Magmatic versus metamorphic origin of olivine-plagioclase coronas. *Contributions to Mineralogy and Petrology* 143, 537-550.

Dickinson, W.R., 2004. Evolution of the North American Cordillera. *Annu. Rev. Earth Planet. Sci.* 32, 13-45.

Ford, H.A., Fischer, K.M., Lekic, V., 2014. Localized shear in the deep lithosphere beneath the San Andreas fault system. *Geology* 42, 295-298.

Fossen, H., Cavalcante, G.C.G., 2017. Shear zones–A review. *Earth-Science Reviews* 171, 434-455.

Gastil, R.G., Phillips, R.P., Allison, E.C., 1975. Reconnaissance geology of the state of Baja California. Geological Society of America.

Gordon, R.G., 1998. The plate tectonic approximation: Plate nonrigidity, diffuse plate boundaries, and global plate reconstructions. *Annual Review of Earth and Planetary Sciences* 26, 615-642.

Henstock, T.J., Levander, A., Hole, J.A., 1997. Deformation in the lower crust of the San Andreas fault system in northern California. *Science* 278, 650-653.

Holtzman, B.K., Kendall, J.M., 2010. Organized melt, seismic anisotropy, and plate boundary lubrication. *Geochemistry, Geophysics, Geosystems* 11.

Joesten, R., 1986. The role of magmatic reaction, diffusion and annealing in the evolution of coronitic microstructure in troctolitic gabbro from Risör, Norway. *Mineralogical Magazine* 50, 441-467.

Kelemen, P.B., Yogodzinski, G.M., Scholl, D.W., 2003. Along-strike variation in the Aleutian island arc: Genesis of high Mg# andesite and implications for continental crust. *Inside the Subduction Factory*, Geophys. Monogr. Ser 138, 223-276.

Kushiro, I., Yoder, H.S., 1969. Melting of forsterite and enstatite at high pressures under hydrous conditions. *Carnegie Inst Washington Yearb* 67, 153-161.

Lanari, P., Vho, A., Bovay, T., Airaghi, L., Centrella, S., 2019. Quantitative compositional mapping of mineral phases by electron probe micro-analyser. Geological Society of London, Special Publications, **478**, 39-63.

Lee, C.-T.A., Harbert, A., Leeman, W.P., 2007. Extension of lattice strain theory to mineral/mineral rare-earth element partitioning: An approach for assessing disequilibrium and

developing internally consistent partition coefficients between olivine, orthopyroxene, clinopyroxene and basaltic melt. *Geochimica et Cosmochimica Acta* 71, 481-496.

Lissenberg, C.J., Dick, H.J., 2008. Melt–rock reaction in the lower oceanic crust and its implications for the genesis of mid-ocean ridge basalt. *Earth and Planetary Science Letters* 271, 311-325.

Lonsdale, P., 1995. Segmentation and disruption of the East Pacific Rise in the mouth of the Gulf of California. *Marine Geophysical Researches* 17, 323-359.

Luhr, J.F., Aranda‐Gómez, J.J., Housh, T.B., 1995. San Quintin volcanic field, Baja California Norte, Mexico: geology, petrology, and geochemistry. *Journal of Geophysical Research: Solid Earth* 100, 10353-10380.

Mainprice, D., Bachmann, F., Hielscher, R., Schaeben, H., 2015. Descriptive tools for the analysis of texture projects with large datasets using MTEX: strength, symmetry and components. Geological Society, London, Special Publications 409, 251-271.

McDonough, W.F., Sun, S.s., 1995. The composition of the Earth. *Chemical Geology* 120, 223-253.

Morris, R.A., DeBari, S.M., Busby, C., Medynski, S., Jicha, B.R., 2019. Building arc crust: plutonic to volcanic connections in an extensional oceanic arc, the southern Alisitos arc, Baja California. *Journal of Petrology* 60, 1195-1228.

Negrete-Aranda, R., Contreras, J., Spelz, R.M., 2013. Viscous dissipation, slab melting, and post-subduction volcanism in south-central Baja California, Mexico. *Geosphere* 9, 1714-1728.

Normark, W.R., Curray, J.R., 1968. Geology and structure of the tip of Baja California, Mexico. *Geological Society of America Bulletin* 79, 1589-1600.

Otamendi, J., Cristofolini, E., Tibaldi, A., Quevedo, F., Baliani, I., 2010. Petrology of mafic and ultramafic layered rocks from the Jaboncillo Valley, Sierra de Valle Fértil, Argentina: implications for the evolution of magmas in the lower crust of the Famatinian arc. *Journal of South American Earth Sciences* 29, 685-704.

Palasse, L., Vissers, R., Paulssen, H., Basu, A., Drury, M., 2012. Microstructural and seismic properties of the upper mantle underneath a rifted continental terrane (Baja California): An example of sub-crustal mechanical asthenosphere? *Earth and Planetary Science Letters* 345, 60-71.

Pikser, J.E., Forsyth, D.W., Hirth, G., 2012. Along-strike translation of a fossil slab. *Earth and Planetary Science Letters* 331, 315-321.

Plattner, C., Malservisi, R., Govers, R., 2009. On the plate boundary forces that drive and resist Baja California motion. *Geology* 37, 359-362.

Rebollar, C., Reyes, A., Reichle, M., 1982. Estudio del enjambre de San Quintin, Baja california, México, ocurrido durante 1975. *Geofísica Internacional* 21.

Rudnick, R.L., Fountain, D.M., 1995. Nature and composition of the continental crust: A lower crustal perspective. *Rev. Geophys.* 33, 267-309.

Satsukawa, T., Ildefonse, B., Mainprice, D., Morales, L., Michibayashi, K., Barou, F., 2013. A database of plagioclase crystal preferred orientations (CPO) and microstructures–implications for CPO origin, strength, symmetry and seismic anisotropy in gabbroic rocks. *Solid Earth* 4, 511-542.

Schmerr, N., 2012. The Gutenberg discontinuity: Melt at the lithosphere-asthenosphere boundary. *Science* 335, 1480-1483.

Soustelle, V., Walte, N.P., Manthilake, M.G.M., Frost, D.J., 2014. Melt migration and melt-rock reactions in the deforming Earth,Äôs upper mantle: Experiments at high pressure and temperature. *Geology* 42, 83-86.

Spencer, J.E., Normark, W.R., 1979. Tosco-Abreojos fault zone: A Neogene transform plate boundary within the Pacific margin of southern Baja California, Mexico. *Geology* 7, 554-557.

Suppe, J., Powell, C., Berry, R., 1973. Regional topography, seismicity, volcanism, and the present-day tectonics of the western United States. Stanford Univ. Pubs. Geol. Sci. 13, 181.

Tharimena, S., Rychert, C., Harmon, N., 2017. A unified continental thickness from seismology and diamonds suggests a melt-defined plate. *Science* 357, 580-583.

Titus, S.J., Medaris Jr, L.G., Wang, H.F., Tikoff, B., 2007. Continuation of the San Andreas fault system into the upper mantle: evidence from spinel peridotite xenoliths in the Coyote Lake basalt, central California. *Tectonophysics* 429, 1-20.

van der Werf, T., Chatzaras, V., Kriegsman, L.M., Kronenberg, A., Tikoff, B., Drury, M.R., 2017. Constraints on the rheology of lower crust in a strike-slip plate boundary: Evidence from the San Quintin xenoliths, Baja California, Mexico. *Solid Earth* 8, 1211-1239.

Wang, Y., Forsyth, D.W., Rau, C.J., Carriero, N., Schmandt, B., Gaherty, J.B., Savage, B., 2013. Fossil slabs attached to unsubducted fragments of the Farallon plate. *Proceedings of the National Academy of Sciences* 110, 5342-5346.

Wilson, C.K., Jones, C.H., Molnar, P., Sheehan, A.F., Boyd, O.S., 2004. Distributed deformation in the lower crust and upper mantle beneath a continental strike-slip fault zone: Marlborough fault system, South Island, New Zealand. *Geology* 32, 837-840.

549 Woodcock, N.H., 1986. The role of strike-slip fault systems at plate boundaries. Philosophical
550 Transactions of the Royal Society of London. Series A, Mathematical and Physical Sciences 317,
551 13-29.

552